

Modulated exponential films generated by surface acoustic waves and their role in liquid wicking and aerosolization at a pinned drop

Daniel Taller,¹ David B. Go,^{1,*} and Hsueh-Chia Chang^{2,*}

¹Department of Aerospace and Mechanical Engineering, University of Notre Dame, Notre Dame, Indiana 46556, USA

²Department of Chemical and Biomolecular Engineering, University of Notre Dame, Notre Dame, Indiana 46556, USA

(Received 13 March 2013; published 9 May 2013)

The exponentially decaying acoustic pressure of scattered surface acoustic waves (SAWs) at the contact line of a liquid film pinned to filter paper is shown to sustain a high curvature conic tip with micron-sized modulations whose dimension grows exponentially from the tip. The large negative capillary pressure in the film, necessary for offsetting the large positive acoustic pressure at the contact line, also creates significant negative hydrodynamic pressure and robust wicking action through the paper. An asymptotic analysis of this intricate pressure matching between the quasistatic conic film and bulk drop shows that the necessary SAW power to pump liquid from the filter paper and aerosolize, expressed in terms of the acoustic pressure scaled by the drop capillary pressure, grows exponentially with respect to twice the acoustic decay constant multiplied by the drop length, with a universal preexponential coefficient. Global rapid aerosolization occurs at a SAW power twice as high, beyond which the wicking rate saturates.

DOI: 10.1103/PhysRevE.87.053004

PACS number(s): 47.55.dr, 43.35.Pt, 68.35.Iv, 78.67.Tf

I. INTRODUCTION

Surface acoustic waves (SAWs) are Rayleigh waves that are formed on the surface of piezoelectric crystals when actuated by a radio frequency (rf) interdigitated electrode transducer. Recently, they have become commonplace in microfluidic platforms as SAW-based devices have the unique capability of generating both strong acoustic radiation fields in fluids as well as strong electrostatic fields at the contact line due to the coupling of the SAW and a piezo-induced electric field wave. While the acoustic pressure due to the SAW refracting into the liquid can drive strong streaming flows [1], the electrostatic Maxwell pressure can be used to generate surface nanodrops [2] or charged aerosol [3].

One promising application that takes advantage of the strong SAW-induced acoustic pressure is the coupling of SAW devices to paper-based fluid devices, shown in Fig. 1. The SAW-induced streaming can extract fluid from the paper much faster than typical capillary action and at a constant speed [4,5]. Thus one can envision using the SAW to enhance paper chromatography or to induce mixing and reactive chemistry on the paper itself. Additionally, if the SAW is of sufficient amplitude, the extracted film breaks up, forming aerosols that can be used for pulmonary drug delivery [5,6], mass spectrometry [3,7] analysis of individual proteins and nanoparticles [8,9], or electronic cooling. Using SAW to aerosolize fluid samples has many advantages over more conventional methods, including lower power requirements, no need for nozzles or other orifices, relatively low shear stresses to avoid damaging biological samples, and the ability to reliably produce droplets in the 1–5 μm range, which is critical for pulmonary drug delivery. Thus paper serves as a cheap and low-maintenance medium for sample delivery, but the fluid flow rate is no longer constrained by wetting through the paper medium, which has a velocity that decays in time as

$t^{-1/2}$ [10]. Both the pumping and the aerosolization are tied to a rapid change in the curvature of the extracted film that exists between a thin, undulating surface droplet region near the contact line and the bulk film where the SAW pressure has decayed and a bulk hydrodynamic pressure enhances pumping. This work explores the role the exponentially decaying acoustic pressure has on governing the liquid topology, the transition to aerosolization, and enhanced pumping through the paper.

II. EXPERIMENTAL METHODS

Our SAW devices consist of interdigitated, focusing gold electrodes [11] fabricated on the surface of 127.68° y - x lithium niobate (LiNbO_3) substrates. The devices were operated at a frequency of $f_{\text{SAW}} = 29.5$ MHz (corresponding to wavelength $\lambda_{\text{SAW}} = 132 \mu\text{m}$) and powers ranging from 0 to 6 W using a waveform generator (Agilent 33250A) and linear rf amplifier (E&I 325LA). Fluid was brought to the surface of the SAW device by using a narrow strip (0.5 cm) of clean room paper (TX 609 TechniCloth Nonwoven Wipers) to wick solution from a small reservoir to the surface of the SAW device. The paper was fully saturated with the working solution prior to operation and then brought into contact with the surface of the SAW substrate, bridging the reservoir and SAW device. Profile images of the extracted liquid film and aerosolization were obtained by using a high-speed camera (Photron Fastcam SA4) with a Navitar telescopic lens (~48× magnification) operating at 3600 fps and 1 megapixel resolution. The flow velocity of fluid through the paper wick was found by seeding the paper with a slug of red ink, as shown in Fig. 1, and measuring the distance the ink travels over time using video photography. The working solutions included different mixtures of deionized (DI) water, HPLC grade acetonitrile (Fischer Scientific), glycerol (VWR International), and acetic acid (Sigma-Aldrich). Specific mixture ratios used in this work are specified in the text.

*Corresponding author: dgo@nd.edu or hchang@nd.edu

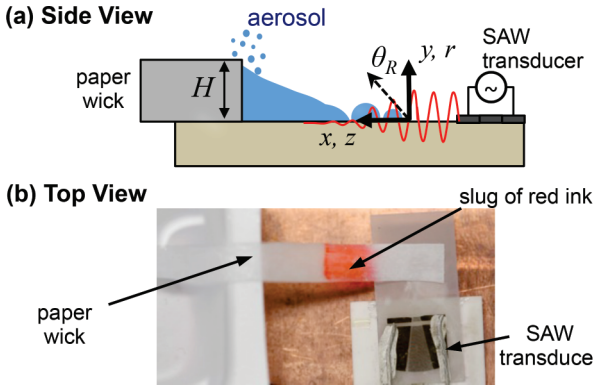


FIG. 1. (Color online) (a) Schematic of SAW device (side view), where the SAW refracts into the liquid film eluting from the paper at angle $\theta_R = 22^\circ$. (b) Measurement of fluid pumping velocity. The paper wick is seeded with a slug of red ink, whose position is tracked over time to yield a velocity measurement.

III. EXTRACTED LIQUID FILM TOPOLOGY AND AEROSOLIZATION REGIMES

The shape of the quasistatic liquid film and its eventual breakup is governed by a balance of capillary pressure (from surface tension) and a local acoustic pressure at the contact line that arises from SAWs refracting from the solid substrate into the liquid at the Rayleigh angle $\theta_R = 22^\circ$. Employing a first-order approximation for fluid velocity u under the action of the surface acoustic waves, a time-averaged dynamic pressure may be computed as $\langle \rho u^2 / 2 \rangle$ [12,13]. With the Cartesian x and y directions defined as shown in Fig. 1(a), the radiated acoustic pressure is

$$P_{\text{acoustic}} = \frac{1}{2} \rho (1 + \alpha^2) A^2 \omega^2 e^{-2(k_x x + k_y y)}, \quad (1)$$

where ρ is the fluid density, $\alpha = 1 / \tan(\theta_R)$ is an attenuation constant arising from the change in speed of the wave from

the solid to the liquid phase, $\omega = 2\pi f_{\text{SAW}}$ is the SAW angular frequency, and A is the amplitude of the SAW wave [13].

The acoustic pressure decays exponentially with decay constant k_R in the direction of SAW propagation at refraction angle θ_R , so that $k_x = k_R \sin(\theta_R)$ and $k_y = k_R \cos(\theta_R)$. This characteristic spatial attenuation factor, or inverse acoustic decay length, governed by the acoustic mismatch between the solid and liquid phases at the interface, is approximately

$$k_R \approx \rho c / (\rho_s c_s \lambda_{\text{SAW}}) \quad (2)$$

for an unbounded fluid [12,14–16], where $\rho_s = 4650 \text{ kg/m}^3$ and $c_s = 3965 \text{ m/s}$ are the density and the speed of sound of LiNbO₃, respectively [17], and ρ and c are the density and the speed of sound of the liquid. This evaluates to $k_R \sim 600 \text{ m}^{-1}$ for water, but more complete numerical results place $k_R \sim 3000–7000 \text{ m}^{-1}$ [13,18]. In addition, the presence of a finite film height has been experimentally shown to increase the effective decay constant [2]. We thus introduce a scaling constant, $k_R = 7.47 \rho c / (\rho_s c_s \lambda_{\text{SAW}})$, chosen to make the experimental results in the present work more compatible with theory.

Though liquid is constantly extracted from the paper into the liquid film and is then lost to evaporation and aerosolization, the shape of the liquid-air interface remains the same over time, allowing a quasistatic approximation at low SAW power. Our images in Fig. 2 show three distinct regimes: a *quasistable film* regime at low power [Figs. 2(a)–2(c)]; a *weak aerosolization* regime at moderate power, in which capillary waves increase and eventually pinch off near the filter paper edge [Figs. 2(d)–2(f)]; and a *rapid aerosolization* regime at high power, in which the entire extracted film destabilizes and dramatically thins with aerosol produced in a chaotic fashion [Figs. 2(g)–2(i)]. The quasistatic film is observed in the first two regimes as the film profiles show a distinct conic shape with the tip pointing towards the SAW wave. A balance of capillary pressure with acoustic pressure produces a Young-Laplace equation [19,20]

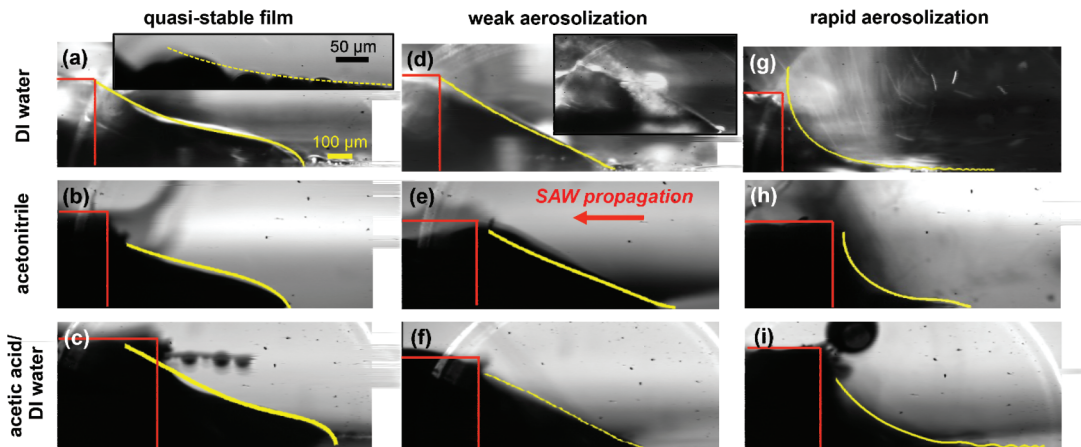


FIG. 2. (Color online) Film regimes under increasing SAW power from left to right. (a)–(c) Quasistable film regime (no aerosol). The inset shows a closeup view of the acoustic droplets and their exponential envelope from the theory. (d)–(f) Weak aerosolization regime. Initial film rupture occurs and droplet emission takes place near the filter paper. The inset shows a discrete aerosolization event. (g)–(i) Rapid aerosolization regime, in which the film has thinned and aerosol emission occurs near the contact line. Numerical solutions are overlaid in yellow and match the topology closely. The filter paper is outlined in red on the left. The working solutions were DI water (top row), acetonitrile (middle row), and 40% acetic acid-DI water by volume (bottom row).

for the quasistatic axisymmetric cone:

$$\gamma \frac{1}{r} \frac{d}{dr} \left\{ r \frac{dz/dr}{[1 + (dz/dr)^2]^{1/2}} \right\} = \frac{1}{2} \rho(1 + \alpha^2) A^2 \omega^2 e^{-2(k_x z + \alpha k_x r)} + P_o, \quad (3)$$

where γ is surface tension, r is the radius of the liquid film, and z is the depth into the fluid. P_o is a parameter representing the hydrodynamic pressure difference between the liquid and the surrounding atmospheric pressure. Close to the contact line, P_o is unimportant because of the relative strengths of the high acoustic and capillary pressures. However, the hydrodynamic pressure induced at the contact line is crucial in determining the film curvature far from the contact line in the bulk of the film near the filter paper, where the exponentially decaying acoustic pressure vanishes. Further, when P_o is negative, meaning that it is less than the ambient pressure, liquid is pumped through the filter paper. This parameter thus determined the SAW-induced liquid pumping rate.

Solutions to Eq. (3) are required to satisfy the “far-field” condition that $r = H$ at $z = L$, where $H = 0.5\text{mm}$ is the height of the filter paper. From observation, $L \sim 2H$ is the length of the extracted liquid film for a LiNbO_3 substrate cleaned with acetone and allowed to dry prior to each experiment. It should be noted that this length may vary greatly with surface treatment of the substrate, becoming as large as $10H$ for a hydrophilic surface treatment with oxygen plasma and less than H for a hydrophobic treatment with trichloro(1H,1H,2H,2H-perfluoroctyl)silane via evaporation. In addition, we impose a vertical slope (90° contact angle) at the contact line $r = z = 0$ to avoid a singular curvature. Equation (3) may then be solved numerically, adopting an arclength-angle formulation [19,20] in terms of the arclength ds taken along the liquid-air interface and the inclination angle φ of the solution curve with respect to the r axis, so that $dr = \cos(\varphi)ds$ and $dz = \sin(\varphi)ds$. We render the equation dimensionless with a normalized axial distance $\tilde{z} = z/H$, radius $\tilde{r} = r/H$, decay constant $k^* = k_x H$, SAW pressure magnitude $B^* = \frac{1}{2} \rho(1 + \alpha^2) A^2 \omega^2 / (\gamma/H)$, and hydrodynamic bulk pressure $P_o^* = P_o / (\gamma/H)$. Equation (3) may then be rephrased as $d\varphi/d\tilde{s} = -\sin(\varphi)/\tilde{r} + B^* e^{-2k^*(\tilde{z} + \alpha\tilde{r})} + P_o^*$, where P_o^* is selected via the shooting method to construct a solution consistent with the prescribed boundary conditions. The shape of the bulk drop is captured accurately, as seen in Fig. 2.

Additionally, the model generally predicts acoustic droplets near the contact line in addition to a bulk film, as pictured in Fig 2(a) (main image and inset) and also described in detail by Taller *et al.* [2]. However, experiments show more acoustic droplets present at lower powers than predicted by Eq. (1). The arbitrary condition of vertical slope at the contact line changes the number of acoustic droplets predicted in the modulated film but does not affect the bulk film except at zero acoustic decay constant. It can, in principle, be relaxed with Maxwell pressure, disjoining pressure, or a molecular scale precursor film [2,19,21,22]. It should be noted that the acoustic droplets are more difficult to experimentally capture in still profile images with solutions such as acetonitrile and acetic acid mixtures due to the rapid evaporation and re-formation of the droplets. See

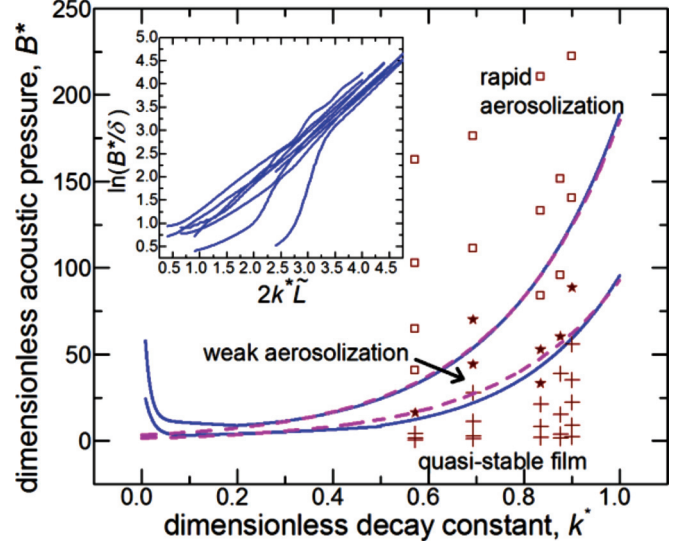


FIG. 3. (Color online) Phase diagram of SAW-induced liquid film regimes for different nondimensionalized SAW pressures B^* and decay constants k^* . The working solutions, from lowest to highest decay constant, acetonitrile, DI water, 10% acetic acid-DI water by volume, 40% acetic acid-DI water by volume, and 11% glycerol-DI water by volume. Pluses indicate the quasistable film regime (no aerosol), stars indicate the weak aerosolization regime with initial film rupture and droplet emission, and squares indicate the rapid aerosolization regime. The solid blue lines are the numerical phase boundaries. The dashed magenta lines show the $B^* \sim \delta e^{2k^*L}$ scaling derived via asymptotic analysis, with $\delta_{\text{weak}} = 1.7$ and $\delta_{\text{rapid}} = 3.4$ for the weak and rapid aerosolization phase boundaries. The inset collapses the weak aerosolization and rapid aerosolization phase boundaries for $\tilde{L} = 1$ to 4 with the same value of δ_{weak} (δ_{rapid}) used for each weak (rapid) aerosolization boundary.

the Supplemental Material [23] for additional video imagery of these droplets in both acetonitrile and DI water.

The images in Fig. 2 indicate pronounced variations in the film profile with increasing SAW power, particularly in the sign of the film curvature at the paper tip. We hence impose the following mathematical criteria for the boundaries of these various regimes: The transition from the *quasistable film* regime to the *weak aerosolization* regime occurs when there is an inflection point ($d\varphi/d\tilde{s} = 0$) at the filter paper edge, while the onset of *rapid aerosolization* occurs when the liquid profile thins such that it becomes impossible to meet the boundary condition $r = H$ at $z = L$, with the slope becoming infinitely large ($d\tilde{z}/d\tilde{r}$ tending to zero) near the filter paper edge. The numerical phase boundaries thus constructed from (3) demarcate the different aerosolization phases for a variety of liquids in Fig. 3.

We see that when the decay constant k^* becomes large, corresponding to a higher fluid density or a higher speed of sound in the fluid, the pressure provided by the SAW device does not penetrate deeply into the fluid and hence the supplied power required for film breakup and aerosolization increases dramatically. On the other hand, in the singular limit of zero decay constant k^* , there is no decay in the bulk, such that the right-hand side of Eq. (3) becomes constant, leading to a constant liquid curvature. The result is a vertical asymptote at $k^* = 0$ corresponding to a spherical outer drop of constant

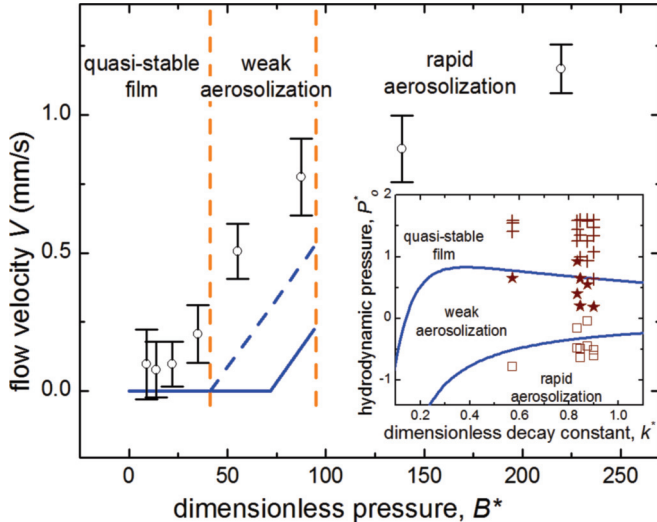


FIG. 4. (Color online) Flow velocity as a function of nondimensionalized SAW pressure B^* for DI water. The solid blue curves show theoretical flow velocity and the vertical dashed orange lines show the computed aerosolization regimes. The oblique dashed blue line shifts the onset of SAW pumping to match the onset of weak aerosolization. Inset shows nondimensionalized hydrodynamic pressure P_o^* used to calculate the flow velocity via the Ergun equation, as a function of the nondimensionalized decay constant k^* . Pluses, stars, and squares are used to indicate the quasistable film regime, weak aerosolization regime, and the rapid aerosolization regime, respectively.

radius. This singular limit for the bulk drop is an artifact of the 90° contact angle, which is no longer “regularized” by the modulated film. There is also an intermediate region of interest between the large and small k^* limits, where the acoustic decay length is roughly the order of the filter paper height. Numerical solution of Eq. (3) also determines the hydrodynamic pressure P_o^* (Fig. 4 inset) and we find that it can in fact be negative. Again, we observe a singular vertical asymptote at $k^* = 0$ where a negative hydrodynamic pressure P_o^* must balance the high SAW pressure B^* to assure a constant curvature. For larger k^* , the hydrodynamic pressures at weak and rapid aerosolization both approach constant asymptotes. In this limit, the decay of SAW pressure becomes more severe and the hydrodynamic pressure away from the contact line becomes insensitive to changes in power and decay constant. We shall develop a universal scaling theory using this invariance.

IV. SAW-INDUCED LIQUID PUMPING

We can estimate the SAW-induced flow velocity V using the Ergun equation [24] for pressure driven flow through a porous medium,

$$\frac{150\mu(1-\varepsilon)}{\rho D_p V} + 1.75 = \frac{-P_o}{L_{\text{paper}}} \frac{D_p}{\rho V^2} \left(\frac{\varepsilon^3}{1-\varepsilon} \right), \quad (4)$$

where μ is viscosity, L_{paper} is the length of the filter paper, and $D_p = 20 \mu\text{m}$ is the fiber diameter, consistent with images of the filter paper under magnification. The void fraction ε was determined experimentally by measuring the difference in mass between dry and saturated filter paper of known size and estimating the ratio of liquid volume in the empty pores to

the total volume. Our experimentally estimated value of $\varepsilon \approx 0.83$ was close to the best-fit value of $\varepsilon = 0.88$ obtained from curve-fitting the experimentally obtained pumping speeds.

The predicted flow speeds for DI water, obtained with the numerical value for P_o^* , are compared to the experimental flow speeds measured by observing a slug of red ink moving through the filter paper in Fig. 4. For low powers (small B^*) $P_o^* > 0$ and the analytical model does not predict any flow. But as the applied power increases, a strongly negative curvature develops resulting in a sharp transition where the flow speed increases nearly linearly until the point of rapid aerosolization when the numerical solution breaks down. The transition in P_o^* from a positive to a negative value occurs within the weak aerosolization phase. However, we expect pumping action to ensue even at the onset of this regime to replenish the mass loss due to weak aerosolization. We suspect that a missing negative dynamic pressure due to high-speed flow at the edge exists to reduce P_o^* to zero there. A shift of the theoretical curve to the onset of weak aerosolization (dashed blue line in Fig. 4) shows good correlation with the data. Beyond the weak aerosolization regime, we observe turbulent dissipation in the rapid aerosolization regime which we cannot model with the current quasistatic theory. This sharply increases the pumping power required for further increase in the flow rate. Hence, the onset of rapid aerosolization marks a point of optimal efficiency.

V. ASYMPTOTIC ANALYSIS

The phase boundaries of Fig. 3 can be captured with a scaling theory based on matching the inner modulated film near the contact line, where the acoustic pressure dominates to balance the capillary pressure and the hydrodynamic pressure is negligible, to an outer bulk region near the filter paper edge where capillary pressure is balanced only by the hydrodynamic pressure. Critically, the absence of the acoustic pressure produces large curvature variations in the bulk drop that are responsible for the different aerosolization regimes. This approach hence yields analytical descriptions for the phase boundaries and the cause of the negative hydrodynamic pressure.

The inner region near the contact line, where the dimensionless acoustic pressure B^* is dominant, is described by

$$\frac{1}{\tilde{r}} \frac{d}{d\tilde{r}} \left\{ \tilde{r} \frac{d\tilde{z}/d\tilde{r}}{[1 + (d\tilde{z}/d\tilde{r})^2]^{1/2}} \right\} = B^* e^{-2k^*(\tilde{z} + \alpha\tilde{r})}. \quad (5)$$

While this equation is not integrable, an envelope that bounds the droplets of the inner solution can be derived explicitly, as shown for a modulated pendant cylinder in [19]. This envelope grows exponentially from the contact line in a manner that is the reciprocal of how the acoustic pressure decays, $\tilde{r}_{\text{inner}} \sim \frac{1}{B^*} e^{2k^*\tilde{z}_{\text{inner}}}$, and is favorably compared to the imaged modulated film in Fig. 2(a).

The outer bulk drop, where the acoustic pressure has decayed to the extent that the hydrodynamic pressure P_o^* is dominant, is described by the constant curvature Young-Laplace equation

$$\frac{1}{\tilde{r}} \frac{d}{d\tilde{r}} \left\{ \tilde{r} \frac{d\tilde{z}/d\tilde{r}}{[1 + (d\tilde{z}/d\tilde{r})^2]^{1/2}} \right\} = P_o^*, \quad (6)$$

which can be integrated to yield

$$\tilde{z}_{\text{outer}} = \int_{\tilde{r}_{\text{outer}}}^1 \left(\frac{P_o^* \tilde{r}^2}{2} + C \right) \left[\tilde{r}^2 - \left(\frac{P_o^* \tilde{r}^2}{2} + C \right)^2 \right]^{-1/2} d\tilde{r}, \quad (7)$$

where \tilde{z}_{outer} is measured from the filter paper edge and C is a constant of integration. For the transition from a quasistable film to weak aerosolization, which occurs where there is an inflection point at the filter paper edge, the outer solution yields $P_o^* = 2C$. Similarly, for the transition to rapid aerosolization where $d\tilde{z}/d\tilde{r} = 0$ (vertical slope) at the filter paper edge, the outer solution yields $P_o^* = -2C$ at rapid aerosolization.

We connect these inner and outer solutions to form an approximate global solution by imposing matching conditions in the slopes and film heights at an intermediate point. Matching \tilde{r} and in $d\tilde{z}/d\tilde{r}$ for the inner exponential asymptote to (7) at \tilde{r}_m leads to

$$\left(\frac{P_o^* \tilde{r}_m^2}{2} + C \right) \left[\tilde{r}_m^2 - \left(\frac{P_o^* \tilde{r}_m^2}{2} + C \right)^2 \right]^{-1/2} = \frac{1}{2k^* \tilde{r}_m}. \quad (8)$$

We also require that the length of the liquid film, defined as $\tilde{z}_{\text{inner}}(\tilde{r}_m) + \tilde{z}_{\text{outer}}(\tilde{r}_m) = \tilde{L}$, is constant. The length of the inner solution \tilde{z}_{inner} is obtained by inverting the exponential envelope and evaluating the result at \tilde{r}_m while the length of the outer solution \tilde{z}_{outer} at \tilde{r}_m is obtained directly from Eq. (3), producing

$$\begin{aligned} & \frac{1}{2k^*} \ln(B^* \tilde{r}_m) + \int_{\tilde{r}_m}^1 \left(\frac{P_o^* \tilde{r}^2}{2} + C \right) \\ & \times \left[\tilde{r}^2 - \left(\frac{P_o^* \tilde{r}^2}{2} + C \right)^2 \right]^{-1/2} d\tilde{r} = \tilde{L}. \end{aligned} \quad (9)$$

We note that at the weak aerosolization transition, the outer solution resembles a linear cone, albeit with a different angle from the modulated conic film at the inner solution. This implies that the slope is nearly constant in the outer conic drop and the second term, corresponding to $\tilde{z}_{\text{outer}}(\tilde{r}_m)$, can be approximated using the slope at the matching point from Eq. (8). The integral may then be evaluated as

$$\begin{aligned} & \int_{\tilde{r}_m}^1 \left(\frac{P_o^* \tilde{r}^2}{2} + C \right) \left[\tilde{r}^2 - \left(\frac{P_o^* \tilde{r}^2}{2} + C \right)^2 \right]^{-1/2} d\tilde{r} \\ & \approx \int_{\tilde{r}_m}^1 \frac{1}{2k^* \tilde{r}} d\tilde{r} = -\frac{1}{2k^*} \ln(\tilde{r}_m), \end{aligned} \quad (10)$$

indicating growth in the outer solution in a manner similar to the exponential inner asymptote but *insensitive* to acoustic pressure. Thus $\tilde{z}_{\text{inner}}(\tilde{r}_m) + \tilde{z}_{\text{outer}}(\tilde{r}_m) = \tilde{L}$ can be

approximated by

$$\frac{1}{2k^*} \ln(B^* \tilde{r}_m) - \frac{1}{2k^*} \ln(\tilde{r}_m) = \tilde{L}. \quad (11)$$

Equation (11) shows that $B^* \sim e^{2k^* \tilde{L}}$, so that the phase boundary inherits the inverse of the exponential form of the acoustic pressure without dependence on the matching location \tilde{r}_m . This imprint of the SAW exponential decay arises because the conic drop of the outer region at weak aerosolization stipulates that the inner solution at the contact line ($\tilde{z} = 0$) must have a slope that can be extrapolated to the filter paper. It should be noted that the analysis presented above does not capture the difference between the weak aerosolization and rapid aerosolization phase boundaries. This is due to the fact that the matching relies upon the continuity in position and slope (first derivative) without reference to changes in higher order derivatives or in the curvature, which are crucial in distinguishing between these two regimes as seen in the profiles in Fig. 2. Without higher order matching, the pronounced curvature for rapid aerosolization would correspond to a higher coefficient in front of the universal scaling compared to weak aerosolization with its near-zero curvature. In fact, exact scalings of $B^* \sim 1.7e^{2k^* \tilde{L}}$ for the weak aerosolization phase boundary and $B^* \sim 3.4e^{2k^* \tilde{L}}$ for the rapid aerosolization phase boundary are obtained using a best fit of the collapsed curves in the inset of Fig. 3, which are evaluated for \tilde{L} ranging from 1 to 4. Both scalings are shown in Fig. 3 to be in quantitative agreement with the full numerical solution to Eq. (3) and with the experimental data.

VI. CONCLUSION

In this work, a model based on the balance of time-averaged acoustic, hydrodynamic, and capillary pressures correctly predicts the topology of the SAW-induced liquid film, the pumping rate, and the transition to aerosolization. In addition, an asymptotic matching approach elucidates how the exponentially decaying acoustic pressure generates a negative hydrodynamic pressure in the bulk film to induce fast pumping. With this work, aerosolization regimes may be predicted analytically as a function of applied power and fluid properties. The model constructed in this paper lays the groundwork for improvements in SAW-based mass spectrometry, pulmonary drug delivery, and other applications.

ACKNOWLEDGMENTS

D.T. wishes to acknowledge the Arthur J. Schmitt Foundation for their generous funding, Ming K. Tan for fabrication of SAW devices, and Sara K. Dale for assistance in image acquisition.

-
- [1] J. Friend and L. Y. Yeo, *Rev. Mod. Phys.* **83**, 647 (2011).
 - [2] D. Taller, D. B. Go, and H.-C. Chang, *Phys. Rev. Lett.* **109**, 224301 (2012).
 - [3] J. Ho, M. K. Tan, D. B. Go, L. Y. Yeo, J. R. Friend, and H.-C. Chang, *Anal. Chem.* **83**, 3260 (2011).
 - [4] A. R. Rezk, A. Qi, J. R. Friend, W. H. Li, and L. Y. Yeo, *Lab Chip* **12**, 773 (2012).
 - [5] M. Kurosawa, A. Futami, and T. Higuchi, in *International Conference on Solid-State Sensors and Actuators, Chicago*, Vol. 2 (IEEE, Piscataway, NJ, 1997), p. 801.

- [6] A. Qi, J. R. Friend, L. Y. Yeo, A. V. Morton, M. P. McIntosh, and L. Spiccia, *Lab Chip* **9**, 15 (2009).
- [7] S. R. Heron, R. Wilson, S. A. Shaffer, D. R. Goodlett, and J. M. Cooper, *Anal. Chem.* **82**, 3985 (2010).
- [8] M. Alvarez, J. Friend, and L. Y. Yeo, *Nanotechnology* **19**, 455103 (2008).
- [9] J. R. Friend, L. Y. Yeo, D. R. Arifin, and A. Mechler, *Nanotechnology* **19**, 145301 (2008).
- [10] E. W. Washburn, *Phys. Rev.* **17**, 273 (1921).
- [11] T.-T. Wu, H.-T. Tang, Y.-Y. Chen, and P.-L. Liu, *IEEE Trans. Ultrason. Ferroelectr. Freq. Control* **52**, 8 (2005).
- [12] D. J. Collins, O. Manor, A. Winkler, H. Schmidt, J. R. Friend, and L. Y. Yeo, *Phys. Rev. E* **86**, 056312 (2012).
- [13] S. Shiokawa and Y. Matsui, *Mater. Res. Soc. Symp. Proc.* **360**, 53 (1994).
- [14] M. Alghane, Y. Q. Fu, B. X. Chen, Y. Li, M. P. Y. Desmulliez, and A. J. Walton, *J. Appl. Phys.* **112**, 084902 (2012).
- [15] J. David and N. Cheeke, *Fundamentals and Applications of Ultrasonic Waves* (CRC Press, Boca Raton, FL, 2002).
- [16] R. M. Arzt, E. Salzmann, and K. Dransfeld, *Appl. Phys. Lett.* **10**, 165 (1967).
- [17] A. Qi, L. Y. Yeo, and J. R. Friend, *Phys. Fluids* **20**, 074103 (2008).
- [18] S. K. Sankaranarayanan and V. R. Bhethanabotla, *IEEE Trans. Ultrason., Ferroelectr. Freq. Control* **56**, 631 (2009).
- [19] R. Finn, *Equilibrium Capillary Surfaces* (Springer, New York, 1986).
- [20] S. Hartley and R. W. Hartland, *Axisymmetric Fluid-Liquid Interfaces* (Elsevier, Amsterdam, 1976).
- [21] P.-G. de Gennes, F. Brochard-Wyart, and D. Quere, *Capillarity and Wetting Phenomena: Drops, Bubbles, Pearls, Waves* (Springer, New York, 2004).
- [22] S. Kalliadasis and H.-C. Chang, *Phys. Fluids* **6**, 1 (1993).
- [23] See Supplemental Material at <http://link.aps.org/supplemental/10.1103/PhysRevE.87.053004> for additional video imagery of these droplets in both acetonitrile and DI water.
- [24] S. Ergun and A. Orning, *Ind. Eng. Chem.* **41**, 1179 (1949).